3D Microstructure Reconstruction of Casting Aluminum Alloy based on Serial Block-Face Scanning Electron Microscopy

Jiawei Lu[1], Bo Chen[1,2,*], Xianping Liu[1,3], Fei Yang[1], Ian K. Robinson[1,2,4,*]

[1] School of Materials Science and Engineering, Tongji University, Shanghai, 201804, China

[2] London Centre for Nanotechnology, University College London, London, WC1H 0AH, UK

[3] Key Laboratory of Advanced Civil Engineering Materials (Tongji University), Ministry of Education, Shanghai, 201804, China

[4] Brookhaven National Laboratory, Upton, NY 11973, USA

[*] Corresponding authors: Bo Chen, Email: bo.chen@tongji.edu.cn, Tel: +86-21-39526230 and Ian K. Robinson, E-mail: i.robinson@ucl.ac.uk

Abstract

In this work, the inner microstructure of aluminum-silicon casting alloy was experimentally investigated to reveal the spatial morphology and phase distribution. Its industrial use is as a light-weight structural material. As a powerful three-dimensional (3D) imaging tool at the nano-scale, the serial block-face scanning electron microscopy (SBF-SEM) was employed to investigate the specimens. After being 3D reconstructed, the images were visualized to identify preference for several specific intermetallics, by quantitative analysis. It was found that these phases have certain relationships in spatial distribution and differences in spatial shapes. The spatial distribution of cracks was studied to understand the propagation and growth relationship.

Keywords : Aluminum alloy, Serial block-face scanning electron microscopy (SBFSEM), 3D microstructure reconstruction, Spatial morphology, Crack propagation

1. **Introduction**

Casting aluminum alloys plays a critical role of substitution of conventional metal materials in the aerospace, automotive, shipbuilding and other machine manufacturing fields. Alloys are chosen for their excellent castability and high strength to weight ratio. Among the casting aluminum alloys, Aluminum-silicon alloy is one of the most widely used.

It is well-known that almost all the performance characteristics of heterogeneous materials is attributed to their microstructural features. Because of the complex microstructure and large amounts of defects, different kinds of casting aluminum alloy vary significantly in certain mechanical properties.

Many previous investigations have addressed the relationship between microstructure and mechanical performance of aluminum-silicon alloy . Xiangqun Ding found the mobility of defects and stress concentration are closely related in the Al-Mg-Si alloys inner microstructure[1]. Mohamed Iben Houria thought secondary dendritic arm spacing has a significant influence on the fatigue age of certain aluminum alloys under the torsional loading condition[2]. Chen found with increasing the size and number of Si particles, interface peeling between particles and matrix appears frequently, which reduces the resistance to fatigue cracks[3]. The spatial distribution of coarse-grained particles, as well as their size and volume fraction in the Al matrix, affects the strength of the composite[4]. Ganesh and Chawla experimentally investigated the influence of Si particle orientation on the fatigue and tensile properties[5] and Campbell found fatigue cracks

always originates from pores and shrinkage defects[6]. Payne found that the microstructure of coarse second phase particles with large area significantly affects the crack initiation[7].

Most of the structure research, such as those reported above, were based on the two dimensional section obtained by conventional methods, such as the Metallographic Microscope, or Scanning Electron Microscope (SEM). For the quantitative characterization of size, shape, connectivity and spatial distribution of pores, grains and intermetallic compounds, it would be very helpful if the data in vertical direction (z axis) was statistically significant too. Some researchers made quantitative assessment of 3D microstructures from a few 2D image sections with a statistical synthetic model[8],but it didn't really return 3D information. So it is inaccurate and unrepresentative to estimate the spatial microstructure information by stereological methods.

A method that can reveal a material in its entirety is quite necessary. So the Three-Dimensional Microstructure Imaging Technique(3D-MIT) has been developed in aluminum alloy researching field. Typically, 3D-MIT is divided into two kinds of classifications according to whether the sample is destroyed or not during the test. One is nondestructive, such as X-ray Computed Tomography based on the energy absorption projections[9,10]. The other one called serial sectioning tomography is destructive, which use different mechanical methods to obtain serial section images. Focused ion beam(FIB), metallographic serial polishing(MSP, serial block-face(SBF) are three applied imaging modalities. FIB is expensive, observable area is too small for region of interest and it may result in sample damage during direct milling by high-energy ions[11,12]. MSP is low cost but its mechanical damage is too much and resolution(in z axis) is not enough for nano/micro scale investigation[13-15]. Considering the balance between area of observed region and influence of mechanical damage during test, here, the 3D detailed features of Al-Si casting alloy was imaged by Serial block-face scanning electron microscope(SBFSEM), which uses a scanning electron microscope with a built-in serial sectioning ultramicrotome for collect high-quality, high-resolution serial images[16,17]. Hashimoto et al have highlighted the strategies for minimizing artifacts caused by SBF system and acquired many 3D images for a variety of metallic and coated systems [19,20]. To realize the 3D microstructure visualization, reconstruction from approximately continuous 2D information is a key process where many algorithms were applied, such as filtering, binarization, thresholding. A particular focus of this study is on the quantitative analysis of critical structural parameters of Al-Si casting alloy, which possibly could enable manufacturing process optimization and numerical investigation for the improvement of mechanical performance in the future.

2. Experimental

The chemical composition of the Al-Si casting alloy investigated in this study is given in Table 1. Samples with the same casting process and heat treatment, "T6 conditions", were used in this experiment. A series of uniaxial strain-controlled fatigue tests were conducted on the samples at the strain amplitude of 0.3 and frequency of 1 hertz. The samples were then observed by Zeiss Sigma 300VP scanning electron microscope (SEM) equipped with an energy-dispersive analysis detector (EDS). SEM tests are operated at 20 kV. Zeiss Sigma 300VP scanning electron microscope (SEM) equipped with Gatan 3-view chamber[Figure 1], one inside ultramicrotomy system named as serial block-face, was used to section samples and image serially prior to reconstructing 3D

images.

Sample preparation is a challenge for Serial block-face scanning electron microscope(SBFSEM) test. The Al-Si aluminum alloy samples were firstly wire cut to shape of strip with size of 1*1*10mm. For ruling out the cutting damage and getting an appropriate shape, conventional ultramicrotomy with a glass knife, LeicaEM UC7, was used to reshape a strip to a cascade quadrangle, as shown in figure 1, whose minimum section area is approximately 300*300um. Then adhere the sample to a one-off sample stage with super glue and conductive silver glue. Ultramicrotomy can cause artificial defects due to pulling off the hard phase or compression of the soft phases [18]. So, before recording the images in SBFSEM, we removed the residual damage generated during the sample preparation by approach operation. In order to minimize the artifact and achieve the better resolution in z axis[19], 0.2 mm/s cutting speed and 30nm slices thickness were set up to the record process. The typical observation conditions were at an acceleration voltage of 2 keV. Finally, choose a representative region of the microstructure with appropriate brightness, contrast and magnification. Selection of this region of interest is vital, which decides whether the image data is valuable or not. It is desirable to capture complete research objects encompassed in the selected volume, which can be reconstructed to 3D and quantitative analysis.

3. **Discussion and Result**

3.1 Intermetallics and other compounds

Because of the incident and inevitable systematic error during the imaging process, a series of preprocessings including alignment, contrast matching, filtering are carried out to the original images for segmentation which is to separate the region of interest from the matrix through specific gray thresholding. Thus, it's essential to exactly identify what each phase with different gray value is. The various intermetallic phases, were identified in this paper by BSE gray value/average atomic number curve, distribution characteristic, morphology feature. To reconstruct the separated regions, volume rendering and surface generating was used to stack slices and visualize the 3D structure. To quantitatively analyze the microstructure, each individual object was labeled and sequences of measured data of labeled objects could be measured by specific algorithm.

On the one hand, EDS can't be employed when the SBF-SEM is working, on the other the observed phases can't be found and tested by EDS after the BSE images collecting due to the destructive experiment process. Under the premise of knowing the existing phases in this alloy, one method was used to identify which intermetallics the different phases in the BSE images are by the relationship among average atomic number, BSE coefficient and gray scale value[20]. In this study, several known intermetallics and silicon compounds in this typical casting Al-Si alloy reported in the past[21], Mg_2Si, Al_2Cu, $Al_5Mg_8Si_6Cu_2$, $Al_{15}(Mn,Fe)_3Si_2$, Al_5FeSi, $Al_8Mg_3FeSi_6$, were inputted to a little python program I wrote. As the result, it calculates values of average atomic number, BSE coefficient and corresponding gray scale ,and plot the graph which was used to deduce the intermetallics in this paper [Figure 2]. But sometimes the gray value of one phase, which is measured from BSE images set, is in a certain range, rather than an exact value because of the systematic error. In this range, we may find more than one intermetallics by observing Figure 2. In this case, an intermetallic can be identified by combining with the reconstructed 3D morphology

because of its certain specific spatial structures.

Al_2Cu

By using a metallurgical microscope, it is easy to determine that the α-Al matrix is separated by the interdendritic network which consists of large amounts of eutectic Si particles and intermetallics[Figure 3].

In Al-Si alloy, one common intermetallic, Al_2Cu, is easy to identified and segmented due to its high contrast relative to other phases within the range between 200-250 in gray value. Being distinguished by spatial shape, Al_2Cu can be classified into two categories: blocky-shaped structure(pro-eutectic) and mesh-shaped structure(eutectic) [Figure 3] Here, two kinds of Al_2Cu in sampleA have been reconstructed to observe their obviously different spatial shapes from overlook map[Figure 4ab]. Restrict by the integrity of the original data, only the blocky-shaped pro-Al_2Cu was completely reconstructed in Z direction relatively[Figure 4c].

In particular, it was found that the eutectic Al_2Cu prefers to fracture into smaller particles along the limited length in z direction, rather than preserve spatial integrity like pro-eutectic Al_2Cu. Each independent block in 2D slices were labeled in different colors by using Avizo 'Labeling' module and enabling the 'XY planes' interpretation. With the slice number increasing, the more colors one slice contains， which means the more separated the phases tend to be[Figure 5].
For each slice, the total area of all the independent phases which are marked in different colors and the counts of independent phases were figured out to plot two graphs [Figure 6] for validating the speculation above. Under the almost same y-scale, the tendency of independent phase number shows the remarkable difference between the two kinds of Al_2Cu. With the decrease of total area of each slice, the independent phase number of mesh-shaped Al_2Cu increases noticeably, while the blocky Al_2Cu always keep stable. From the three-dimensional perspective, the boundary(where total slice area is small) of mesh-shaped Al_2Cu has more branches (independent phases on slices), which means this kind of grain is much coarser than blocky Al_2Cu.

$Al_5Mg_8Si_6Cu_2$

This alloy commonly has as a dominant impurity copper, which forms complex intermetallics during solidification. Solid solution and aging treatments increase the solubility of the eutectic Al_2Cu. Consequently the relative volume fraction of blocky phase (pro-eutectic Al_2Cu) increase to some degree[Figure 3b], which results in some small size phases that was masked by mesh-shaped Al_2Cu is readily disclosed much more apparently[21]. One MgCu-based intermetallic which was reported in acicular or elliptical shape(2D) is $Al_5Mg_8Si_6Cu_2$ which is usually found next to the Al_2Cu phase(both pro-eutectic and eutectic)[22,23]. From the BSE images set, we found one phase whose gray value was measured in the approximate range between 100 and 140 where there are two known compounds, Al_5FeSi and $Al_5Mg_8Si_6Cu_2$ between this range in figure2. Additionally, according to the morphology of this phase, this intermetallic which was found around the blocky Al_2Cu, as shown in Figure 7 is considered to be $Al_5Mg_8Si_6Cu_2$. But from the view of spatial variation, the $Al_5Mg_8Si_6Cu_2$ phase in ellipse actually is not ellipsoid, but similar to elliptic cylinder always carrying a long tail[Figure 8a]. The description of shape in the past (ellipse) may has been misguided due to observing the info-limited 2D section structure, just as shown in Figure 8b(section of overlook).

As for the surrounding of mesh-shaped eutectic Al_2Cu in Figure 9 (which was not completely reconstructed because of the limited data), 'acicular shapes' always appear at the gap between close phases. 'Elliptical shape' is always found to exist in the relatively spacious gap. But in the z direction, these ellipses possibly turn to stripes following a long tail. The spatial morphology of $Al_5Mg_8Si_6Cu_2$ seems to fill the gaps between matrix or other phases, which may suggests the crystallization time of this phase is relatively late.

In my opinion, these two shapes(ellipse or acicular) can be unified to one category, striped-shape, for the large aspect ratio. This is a good example which demonstrates that compared with 2D structure, the 3D structure is more accurate to identify phases.

For the obvious acicular shape structures shown in figure 7a and 7b, quantitative calculations have been done to analysis the spatial morphology. Using labeling module of Avizo by enabling the '3D' interpretation outputs the Figure 7b where each spatially individual particle was highlighted in different color. Spatial geometric statistic of 13 particles have been accurately calculated by using 'label analysis' module based on the reconstructed 3D structure, as shown in the Table2.It is manifest that the length-wide ratio (Feret's diameters was introduced in this statistic) of the particle is positively correlated with its volume[Figure 10]. The correlation coefficient of these two variables is calculated to be 0.565. It is likely that those particles with low length-width ratio and small volume weren't reconstructed completely. Filtering out particles whose volume is smaller than 10^9 nm^3, we found the length-width ratio of remainders (sum of the Length3d / sum of the Width3d) is 5.32.

$Al_{15}(Mn,Fe)_3Si_2$

Around AlMgSiCu phase, another small Fe-containing intermetallic, was found, which has been previously reported[24]. This compound[Figure 11a], $Al_{15}(Mn,Fe)_3Si_2$, was identified by combining the spatial shape of small platelet and the graph achieved above[Figure 2]. The average atomic number and BSE coefficient were calculated to be 18.31 and 0.21 and gray scale range measured in the BSE image[Figure 11b] is between 140-180 which is consistent with the curve in figure 2.

3.2 Cracks and defects

The poor alloy ductility is attributed to the coarse intermetallics, which leads to unsteady crack propagation through a sequence of fracturing events in connecting phases[25]. The following dataset [Figure 12] suggests that the trends of cracks in Al matrix is towards the brittle intermetallics, like Al_2Cu.

When cracks propagate to the intermetallics, three factors are introduced which affect the crack propagation : intermetallic brittleness, defects along grains boundary, intermetallic morphology. When the cracks spread to intermetallics, three common growing types may happen to the cracks, as shown in the Figure 13.

For some intermetallics in plate shape, such as Al_2Cu or $Al_5Mg_8Si_6Cu_2$, crack type 1 happens much more frequently. This is probably because the high brittleness of these phases plays the most

important role in the crack propagation. In this growing type, the crack is always found merely inside the intermetallic, which concluded that the brittle intermetallics act as the crack initiator in general[Figure 14, Figure 15ab]. As to type 2, if the defects gathers along the grains boundary, where defects indeed exist [26], the cracks tend to grow following the boundary because of the stress concentration. Another propagation type 3 illustrates an inductive effect for the zigzag morphology and irregular distribution in small space. As shown in the figure 12, the cracks were found near the eutectic Al_2Cu. Cracks tend to spread following small paths inside the intermetallics[figure 15c]. To a certain extent, these kind of cracks are theoretically restrained by the spatial morphology because the longer propagation distance and more energy are required for crack propagation.

We found in some regions, the cracks tend to concentrate to the brittle phase, the cracks existing in the Al matrix and brittle intermetallics are separated into two colors by the Avizo image logic algorithm[Figure 16a]. It is apparent that the cracks in the brittle phase, which are in purple are much more than in blue which are in Al matrix. Particularly, when numerous cracks appear in one certain brittle phase, it will be normal to find corresponding cracks appearing in the adjacent matrix[Figure 16b]. In the other words, it is very rare that the isolated cracks appear in the aluminum matrix.

A chamfer distance map, an algorithm where each voxel in the region of interest will be assigned a value depending on the distance to the nearest object boundary, was introduced to demonstrate the phenomenon above The boundary voxels of the object are assigned a value of zero whereas the assigned value increases as the distance increases. Applying the distance map algorithm to the binary image of the Al matrix gives a gray level image where each voxel intensity represents the minimal distance in voxels from the matrix envelope which is the boundary between Al matrix and brittle phase[Figure 17a]. Then masking the cracks in the Al-matrix to the distance map gives the distance from each voxel in matrix to the closest voxel in boundary. The counts of voxels in each group which was classified by the distances was plotted in the Figure 17b which shows the number of crack voxels located at a given distance from the matrix envelope. The distance values in voxels are obviously concentrated in the range within 235nm and all the voxels are within 1800nm from the boundary. Consequently, the cracks in the matrix are always close to the brittle phases where cracks have existed. This phenomenon can be explained as follows: once a given intermetallic fractures, the stress relaxation will happen to the surrounding Al matrix, leading to a transfer of load to adjacent matrix[26].

4. Conclusion

The 3D spatial structure of the aluminum-silicon casting alloy sample was revealed by Serial Block-Face Scanning Electron Microscope (SBF-SEM). SBFSEM is a promising characterizing method to be a useful tool to investigate the spatial microstructures of soft alloys. Several specific intermetallics were identified here by their reported morphology and the relationship between Average atomic number, BSE coefficient and gray scale. The spatial shape and distribution of these phases were visualized by 3D reconstruction using Avizo software. Pro-eutectic Al_2Cu is found to have a blocky shape, while the eutectic Al_2Cu tends to be relatively coarser with a mesh-shape. $Al_5Mg_8Si_6Cu_2$ was identified by its striped shape only by inferring its spatial morphology, rather than the past

acknowledge of acicular and elliptical shapes. Gray scale, BSE coefficient and average atomic number were used to identify $Al_{15}(Mn,Fe)_3Si_2$. Based on the spatial distribution data, the propagation and growth law of cracks in this alloy was thought to be concentrated because of the brittle phases and stress transfer. Further quantitative analysis and simulations of the 3D structure could be performed with better original data in the future.

Acknowledgements

This work was supported by the TongJi University, China, through the High-level Talent Programme "Materials Nano-structure" with grant Numbers 152221 and 152243. Work at Brookhaven National Laboratory was supported by the U.S. Department of Energy, Office of Science, Office of Basic Energy Sciences, under Contract No. DE-SC00112704.

Reference

[1]Ding X Q, He G Q, Chen C S. Study on the dislocation sub-structures of Al–Mg–Si alloys fatigued under non-proportional loadings[J]. Journal of Materials Science, 2010, 45(15):4046-4053.

[2]Houria M I, Nadot Y, Fathallah R, et al. Influence of casting defect and SDAS on the multiaxial fatigue behaviour of A356-T6 alloy including mean stress effect[J]. International Journal of Fatigue, 2015, 80:90-102.

[3]Chen Z Z, Tokaji K. Effects of particle size on fatigue crack initiation and small crack growth in SiC particulate-reinforced aluminium alloy composites[J]. Materials Letters, 2004, 58(17–18):2314-2321.

[4]J.G. Kim, J.I. Bang, Y.J. Kim, and Y.H. Park: Korean J. Met.Mater., 2013, vol. 51, pp. 857 – 63.

[5] Chawla N, Sidhu R S, Ganesh V V. Three-dimensional visualization and microstructure-based modeling of deformation in particle-reinforced composites[J]. Acta Materialia, 2006, 54(6):1541-1548.

[6]Gall K, Yang N, Horstemeyer M, et al. The debonding and fracture of Si particles during the fatigue of a cast Al-Si alloy[J]. Metallurgical & Materials Transactions A, 1999, 30(12):3079-3088.

[7]Payne J, Welsh G, Jr R J C, et al. Observations of fatigue crack initiation in 7075-T651[J]. International Journal of Fatigue, 2010, 32(2):247-255.

[8]Park H K, Jung J, Kim H S. Three-dimensional microstructure modeling of particulate composites using statistical synthetic structure and its thermo-mechanical finite element analysis[J]. Computational Materials Science, 2017, 126:265-271.

[9]Rosier D J D, Klug A. Reconstruction of Three Dimensional Structures from Electron Micrographs[J]. Nature, 1968, 217(5124):130-134.

[10]Li G, Shi R, Fan Q, et al. Reconstruction and quantitative characterization of the three dimensional microstructure model of TC6 titanium alloy based on dual-energy X-ray microtomography[J]. Materials Science & Engineering A, 2016, 675:212-220.

[11]Y. Lu, Y.L. Chiu, I.P. Jones. Three-dimensional analysis of the microstructure and bio-corrosion of Mg–Zn and Mg–Zn–Ca alloys[J]. Materials Characterization, 2016, 112:113-121.

[12]Mayer C R, Molina-Aladareguia J, Chawla N. Three dimensional (3D) microstructure-based finite element modeling of Al-SiC nanolaminates using focused ion beam (FIB) tomography[J]. Materials Characterization, 2016, 120:369-376.

[13]Li M, Ghosh S, Rouns T N, et al. Serial Sectioning Method in the Construction of 3-D Microstructures for Particle-Reinforced MMCs[J]. Materials Characterization, 1998, 41(2–3):81-95.

[14]Chawla N, Sidhu R S, Ganesh V V. Three-dimensional visualization and microstructure-based modeling of deformation in particle-reinforced composites[J]. Acta Materialia, 2006, 54(6):1541-1548.

[15]Jung J M, Ji H Y, Jeong H J, et al. Three-Dimensional Characterization of SiC Particle-Reinforced Al Composites Using Serial Sectioning Tomography and Thermo-mechanical Finite Element Simulation[J]. Metallurgical & Materials Transactions A, 2014, 45(12):5679-5690.

[16] Denk W, Horstmann H. Serial block-face scanning electron microscopy to reconstruct three-dimensional tissue nanostructure[J]. Plos Biology, 2004, 2(11):e329.

[17]<http://www.gatan.com/products/sem-imaging-spectroscopy/3view-system>

[18]Chawla N, Sidhu R S, Ganesh V V. Three-dimensional visualization and microstructure-based modeling of deformation in particle-reinforced composites[J]. Acta Materialia, 2006, 54(6):1541-1548.

[19]Hashimoto T, Thompson G E, Zhou X, et al. 3D imaging by serial block face scanning electron microscopy for materials science using ultramicrotomy[J]. Ultramicroscopy, 2016, 163:6-18.
[20]Hashimoto T, Thompson G E, Curioni M, et al. Three Dimensional Imaging of Light Metals Using Serial Block Face Scanning Electron Microscopy (SBFSEM)[J]. Materials Science Forum, 2013, 765:501-505.
[21]HF Lopez.Identification of Intermetallic Phases in an Automotive Grade Aluminum A319 Alloy[J].Materials Performance and Characterization,2017,6:237-255.
[22]Backerud L, Chai G and Tamminen J. Solidification Characteristics of Aluminum Alloys[J]. Foundry Alloys,1990, 2:71-84.
[23]Apelian, D., Shivkumar, S., and Sigworth, G. Fundamental Aspects of Heat Treatment of Cast Al-Si-Mg Alloys[J]. AFS Trans., 1989, 97:727-742.
[24]Puncreobutr, C., Lee, P. D., Kareh, K. M., Connolley, F., Fife, J. L., and Phillion, A. B., Influence of Fe-Rich Intermetallics on Solidification Defects in Al-Si-Cu Alloys[J]. Acta Mater., 2014, 68:42-51.
[25]Wang Q G, Caceres C H. The fracture mode in Al–Si–Mg casting alloys[J]. Materials Science & Engineering A, 1998, 241(1-2):72-82.
[26]Grayson G N, Schaffer G B, Griffiths J R. Fatigue crack propagation in a sintered 2xxx series aluminium alloy[J]. Materials Science & Engineering A, 2006, 434(1–2):1-6.

Figure Captions

Figure1: The inside construction of 3view chamber

Figure2: Line chart of grayscale level, where variation of BSE coefficient with average atomic number and gray scale of intermetallics are contained.

Figure3: Eutectic Al_2Cu and pro-eutectic Al_2Cu were highlighted in the metallurgical image of this investigated alloy

Figure4: Reconstruction image of two kinds of Al_2Cu, the eutectic is in yellow(b), pro-eutectic is in gray(overlook)(a) and green(perspective)(c)

Figure5: The reconstruction images of labeling slices of two kinds of Al_2Cu by enabling the 'XY planes' interpretation (a) is the labeling 3D reconstructive image of eutectic Al_2Cu and the respective slices No.63,55,33,22,0. (b) is the labeling 3D reconstructive image of pro-eutectic Al_2Cu and the respective slices No.530,314,233,134,62,0.

Figure6: The correlative trends between total area and independent phase number in each slice, (a) is eutectic Al_2Cu and (b) is pro-eutectic Al_2Cu.

Figure7:The reconstruction images of $Al_5Mg_8Si_6Cu_2$ which is in acicular shape (a)perspective 3D structure of $Al_5Mg_8Si_6Cu_2$ in acicular shape around pro-eutectic Al_2Cu; (b)each independent $Al_5Mg_8Si_6Cu_2$ particle is marked in different labeling color; (c) Al_2Cu envelope

Figure8: The reconstruction images of $Al_5Mg_8Si_6Cu_2$ which carries a long tail (a)perspective 3D structure of $Al_5Mg_8Si_6Cu_2$ in cylinder shape with long tails; (b)the misleading section characterization like ellipse; (c) Al_2Cu envelope

Figure9:Incomplete 3D structure of $Al_5Mg_8Si_6Cu_2$, which is in blue and around mesh-shaped eutectic Al_2Cu. Some seem like 'acicular shape', the others seem like 'elliptical shape', which were both highlighted in Dotted line frame

Figure10: the Scatter plot of the particles recorded in the table2 regarding the Volume (on log scale) and length-wide ratio.

Figure11:The reconstruction images of $Al_{15}(Mn,Fe)_3Si_2$ which is in the shape of small platelet, (a)3D reconstruction of $Al_{15}(Mn,Fe)_3Si_2$ in red which was surrounded by Al_2Cu (in transparent green) and $Al_5Mg_8Si_6Cu_2$ (in transparent red), (b) one original BSE image of the slices stack

Figure12: The propagation of cracks around the brittle Al_2Cu and $Al_5Mg_8Si_6Cu_2$ in several representative slices, whose trend is marked in red line. Cracks are highlighted in blue, the background is the BSE images.

Figure13: Three types of cracks propagation. The red line represents cracks. Gray objects represent intermetallics with different morphology. (a) represents type 1. (b) represents type 2. Black crosses in (b) represent the defects along the boundary. (c) represents type 3.

Figure14: One original BSE image of the slices stack showing the cracks of type 1

Figure15: The cracks which are marked in blue and theirs distribution in Al matrix(colorless region) and brittleness phase(transparent region which was rendered by Avizo) were visualized in (a). (b) The reconstruction image of crack 'type 1', (c) The reconstruction image of crack 'type 3'.

Figure16: the relationship of the distribution of cracks (a) the separated cracks in two colors: the purple is in brittleness phases and the blue is in the Al matrix. (b) when the cracks appear in the brittleness phase(transparent region), the corresponding cracks always appear in the surrounding matrix(colorless region).

Figure17: the chamfer distance map and the histogram which was plotted by distance map data (a)the distance map illustrates that the greater the gray intensity is, the closer the objects to the boundary (b)Histogram showing the counts of voxels corresponding to the different distances.

Figure1

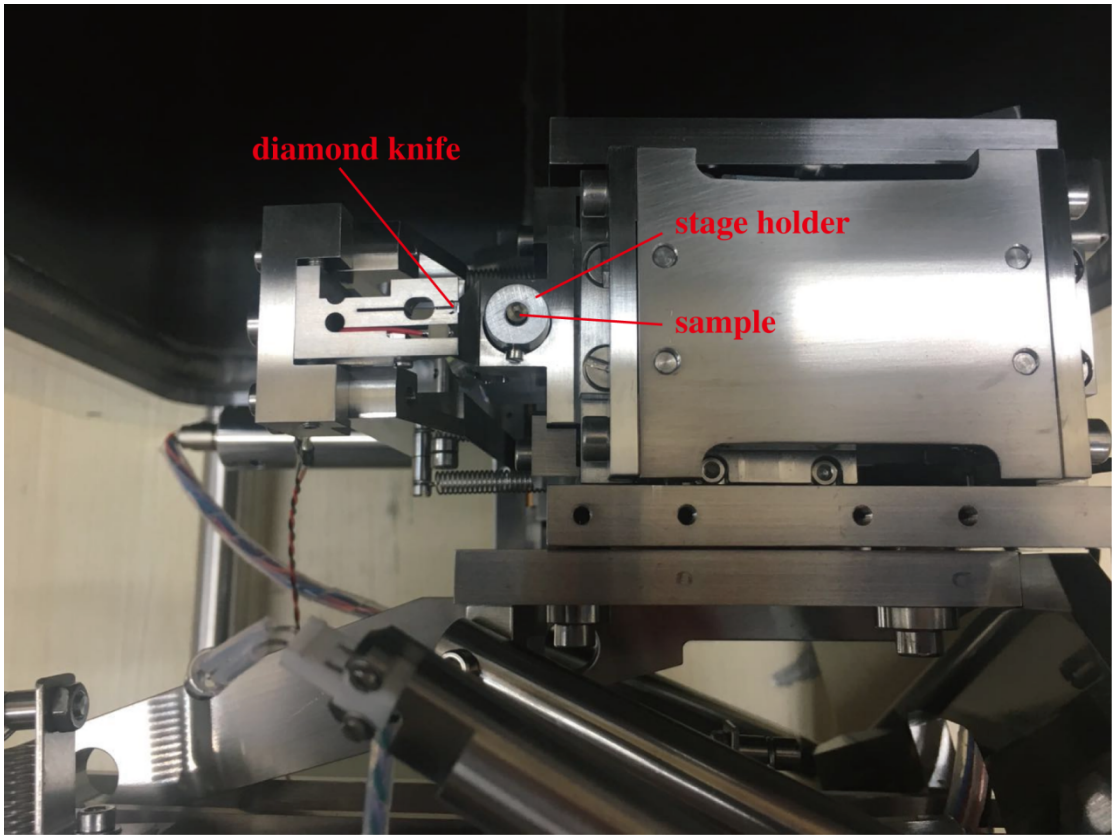

Figure2

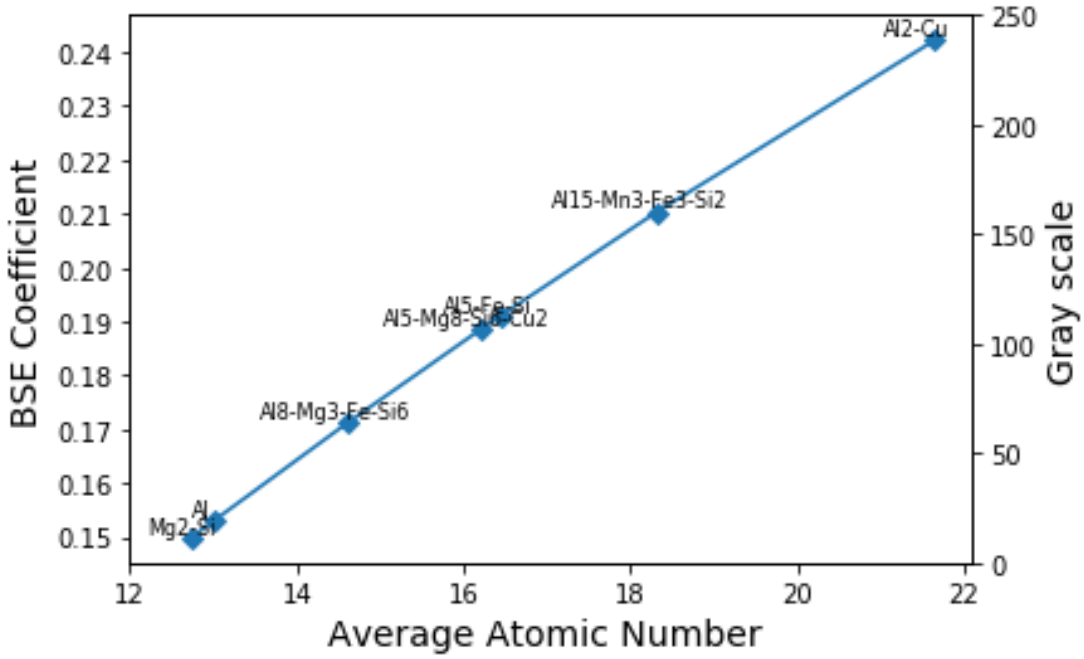

Figure3

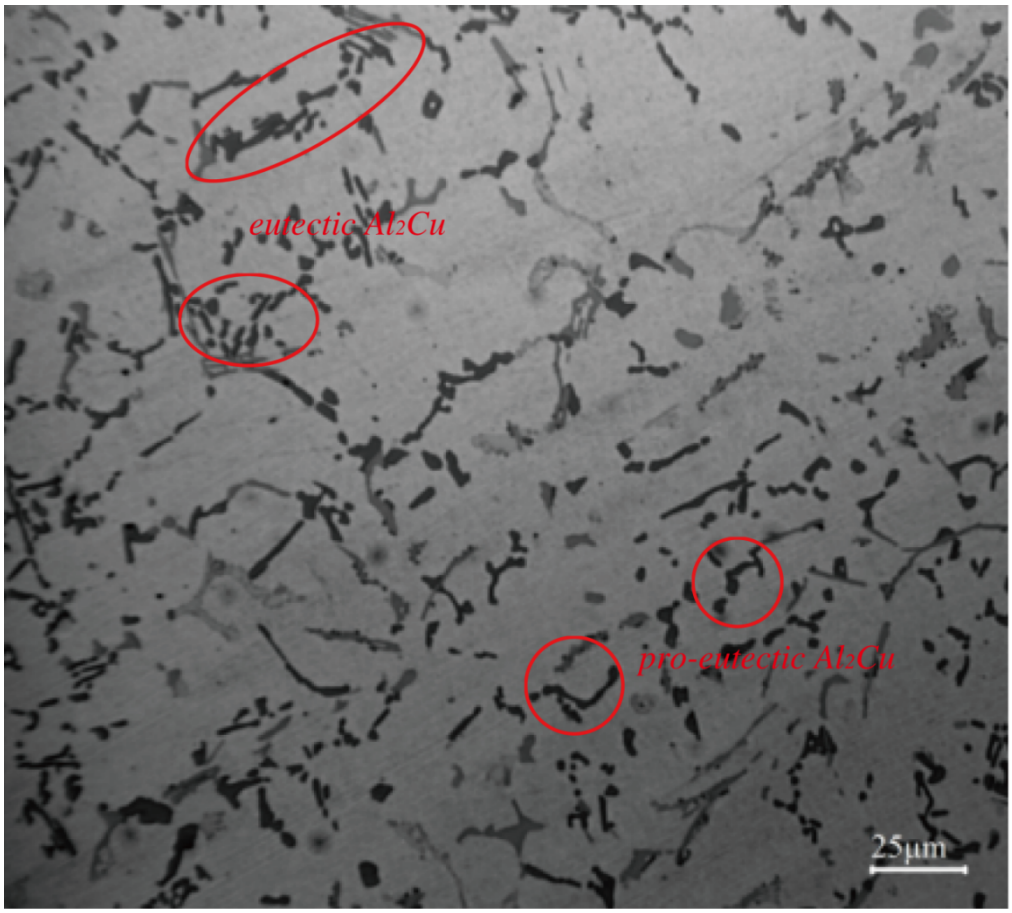

Figure4

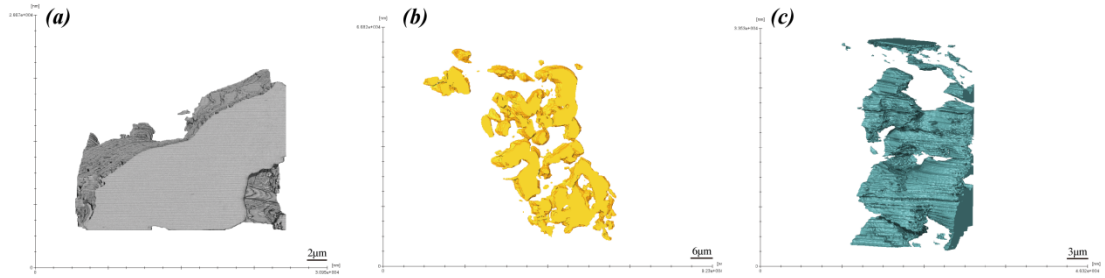

Figure5

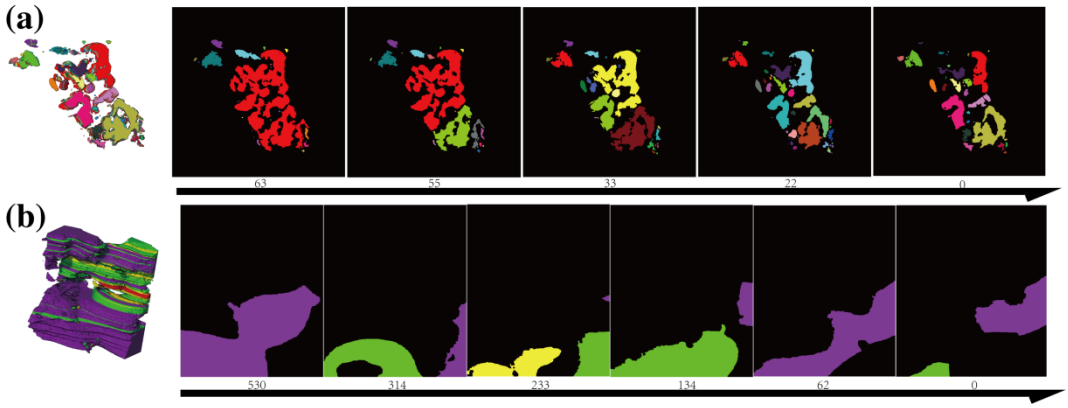

Figure6

(a)

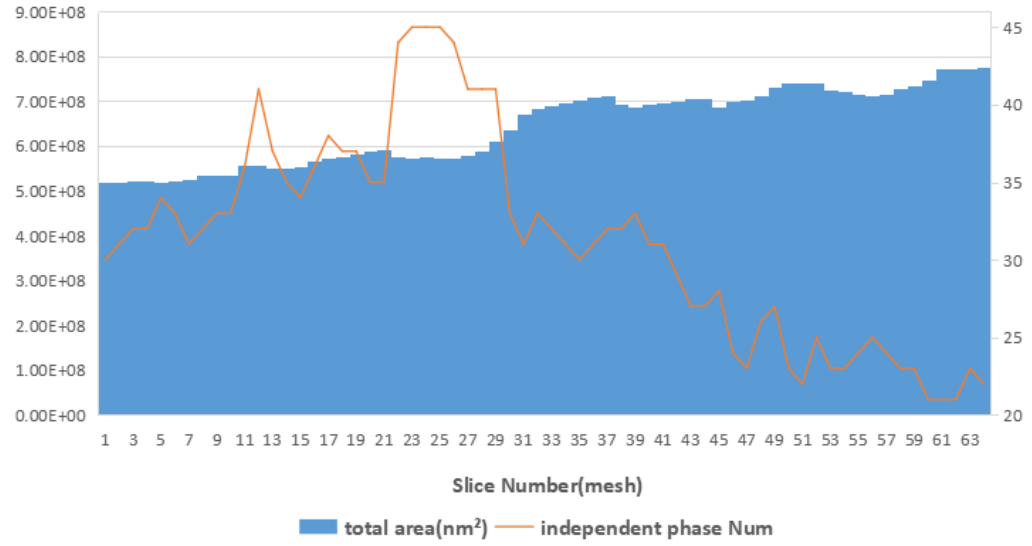
9.00E+08
8.00E+08
7.00E+08
6.00E+08
5.00E+08
4.00E+08
3.00E+08
2.00E+08
1.00E+08
0.00E+00
45
40
35
30
25
20
1 3 5 7 9 11 13 15 17 19 21 23 25 27 29 31 33 35 37 39 41 43 45 47 49 51 53 55 57 59 61 63
Slice Number(mesh)
total area(nm²)
independent phase Num

(b)

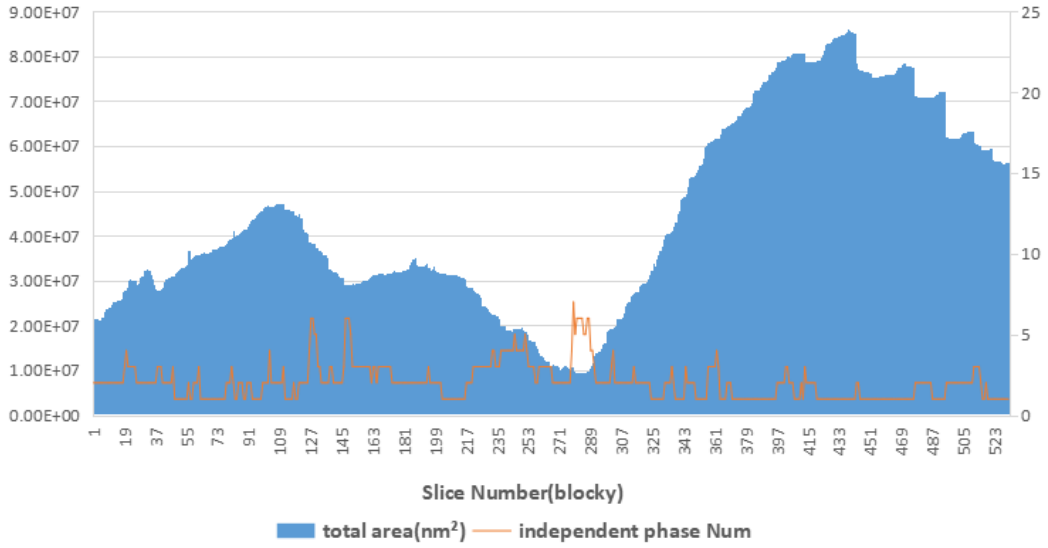
9.00E+07
8.00E+07
7.00E+07
6.00E+07
5.00E+07
4.00E+07
3.00E+07
2.00E+07
1.00E+07
0.00E+00
25
20
15
10
5
0
1 19 37 55 73 91 109 127 145 163 181 199 217 235 253 271 289 307 325 343 361 379 397 415 433 451 469 487 505 523
Slice Number(blocky)
total area(nm²)
independent phase Num

Figure7

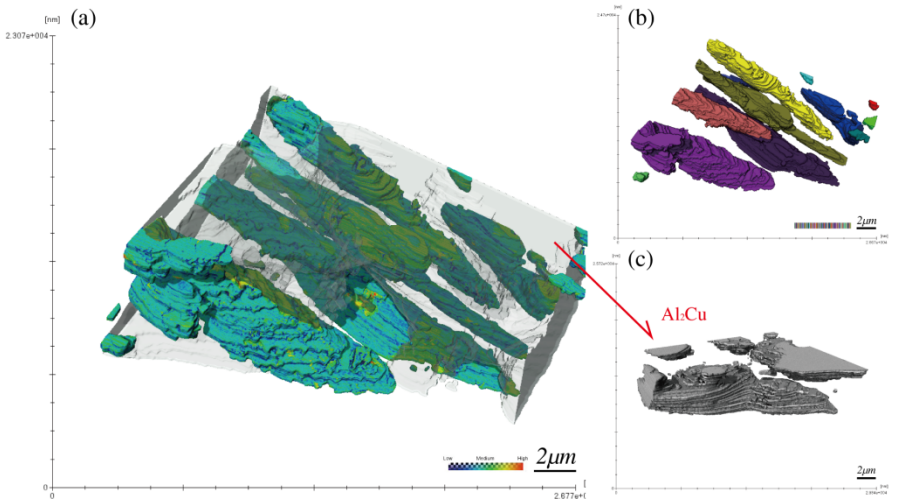

Figure8

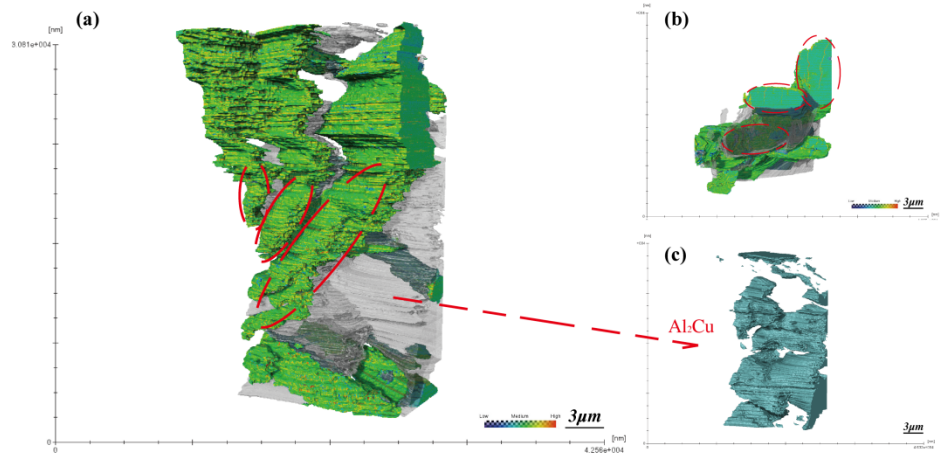

Figure9

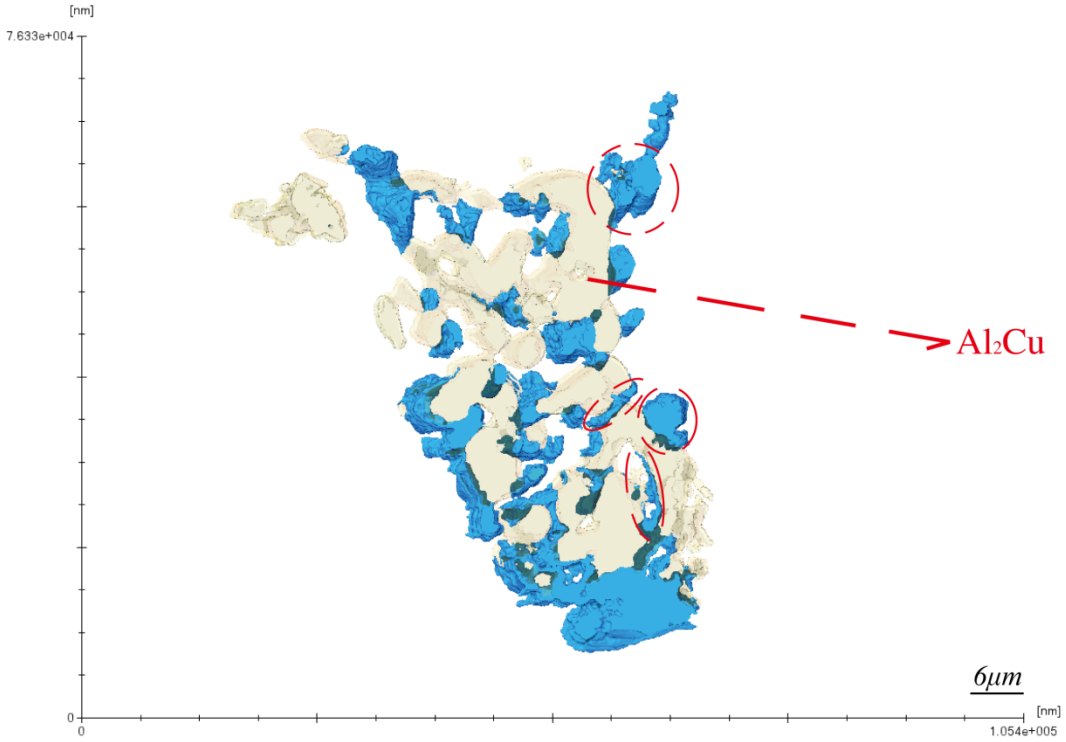

Figure10

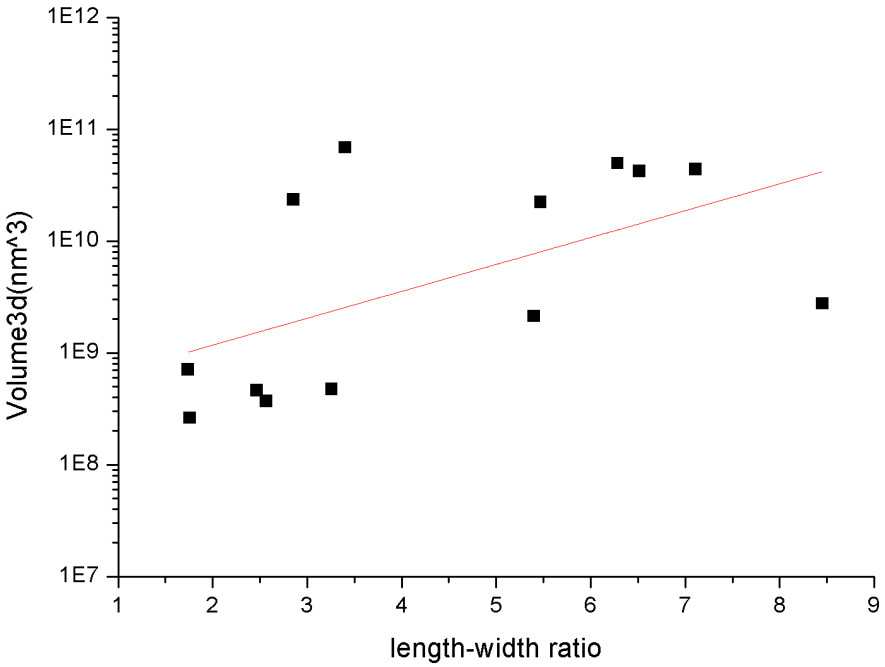

Figure11

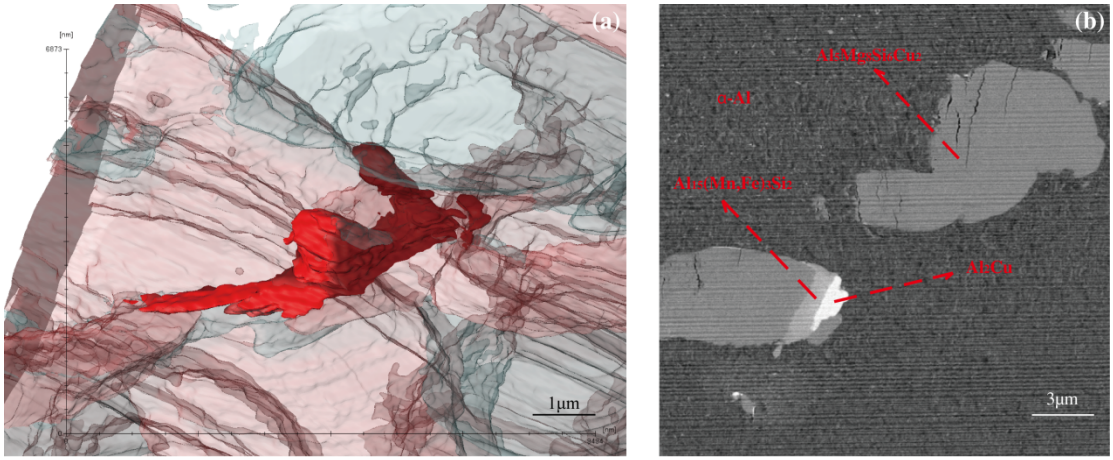

Figure12

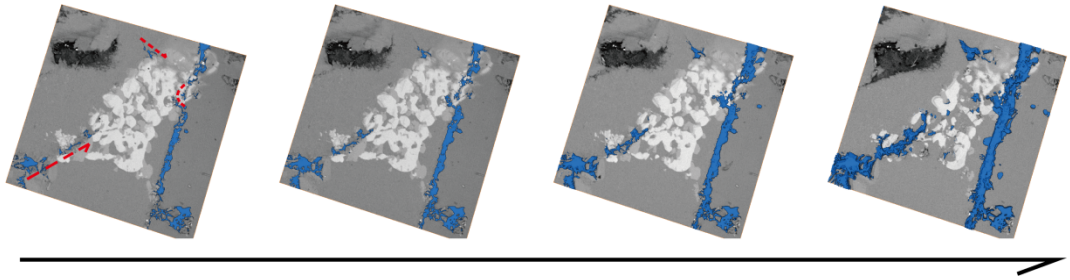

Figure13

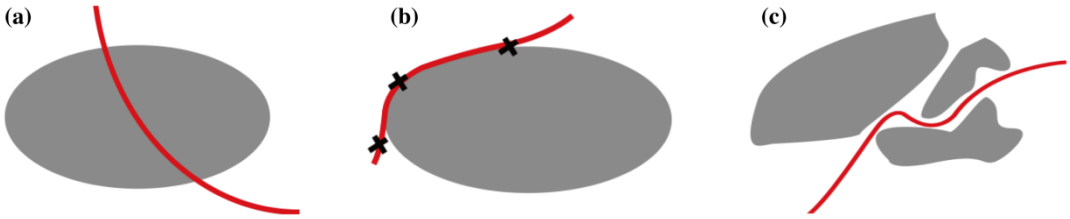

Figure14

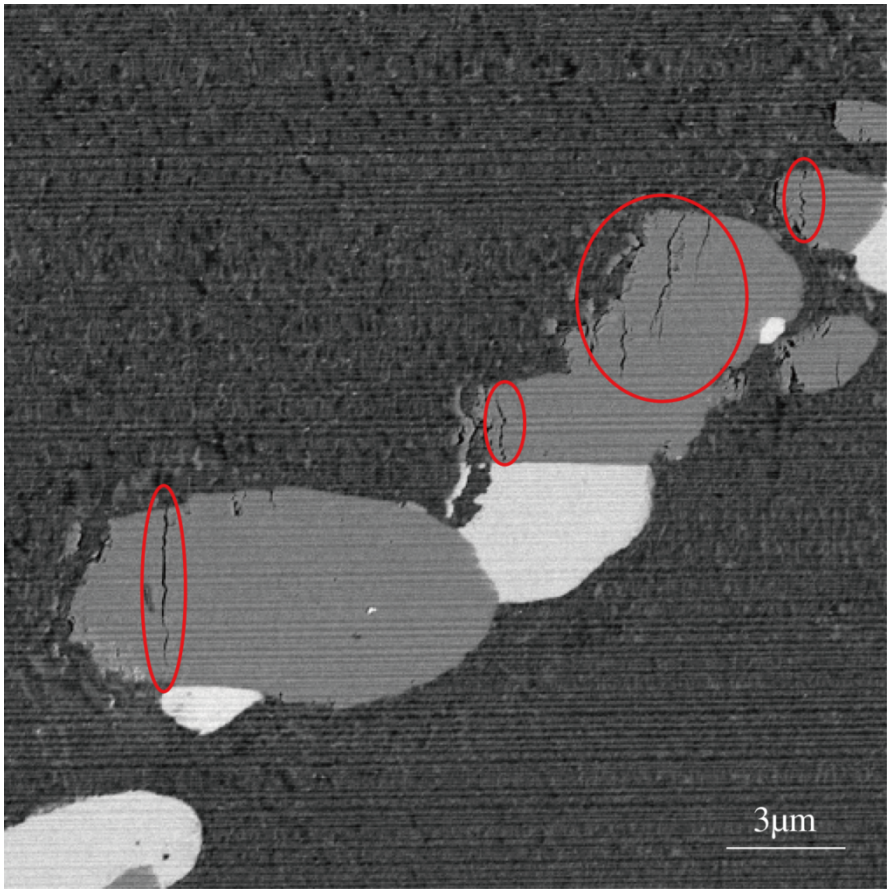

Figure15

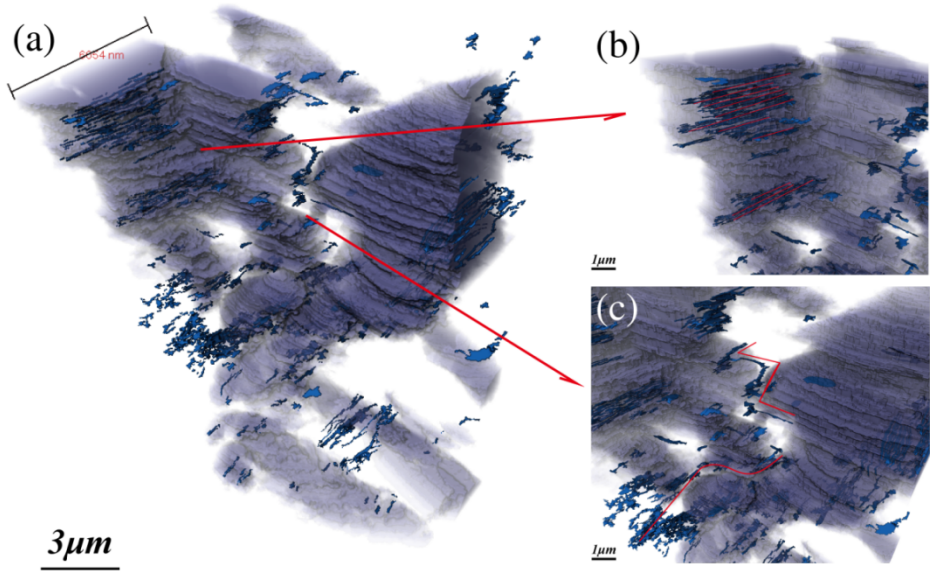

Figure16

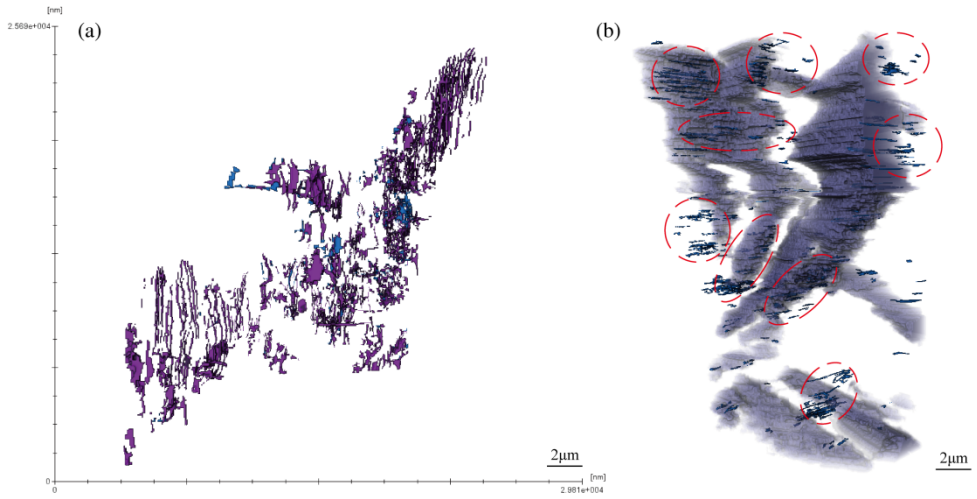

Figure17